2005

Modeling microwave emissions of erg surfaces in the Sahara Desert

Haroon Stephen
University of Nevada, Las Vegas, haroon.stephen@unlv.edu

David G. Long
Brigham Young University - Utah, long@ee.byu.edu

Repository Citation

Modeling Microwave Emissions of Erg Surfaces in the Sahara Desert

Haroon Stephen, *Student Member, IEEE,* and David G. Long, *Senior Member, IEEE*

Abstract—Sand seas (ergs) of the Sahara are the most dynamic parts of the desert. Aeolian erosion, transportation, and deposition continue to reshape the surface of the ergs. The large-scale features (dunes) of these bedforms reflect the characteristics of the sand and the long-term wind. Radiometric emissions from the ergs have strong dependence on the surface geometry. We model the erg surface as composed of tilted rough facets. Each facet is characterized by a tilt distribution dependent upon the surface roughness of the facet. The radiometric temperature (T_b) of ergs is then the weighted sum of the T_b from all the facets. We use dual-polarization T_b measurements at 19 and 37 GHz from the Special Sensor Microwave Imager aboard the Defense Meteorological Satellite Program and the Tropical Rainfall Measuring Mission Microwave Imager to analyze the radiometric response of erg surfaces and compare them to the model results. The azimuth angle (ϕ) modulation of T_b is caused by the surface geometrical characteristics. It is found that longitudinal and transverse dune fields are differentiable based on their polarization difference (ΔT_b) ϕ-modulation, which reflects type and orientation of dune facets. ΔT_b measurements at 19 and 37 GHz provide consistent results. The magnitude of ΔT_b at 37 GHz is lower than at 19 GHz due to higher attenuation. The analysis of ΔT_b over dry sand provides a unique insight into radiometric emission over ergs.

Index Terms—Azimuth angle modulation, ergs, microwave emission, Tropical Rainfall Measuring Mission (TRMM) Microwave Imager (TMI), polarization difference, radiometric temperature, sand dunes, Special Sensor Microwave Imager (SSM/I).

I. INTRODUCTION

THE SAHARA desert is one of the most diverse terrains on Earth and consists of rocky mountains (*hamadas*), boulder and gravel zones (*regs*), and large sand seas (*ergs*) [1]. Erg bedforms are the most dynamic parts of the desert and undergo continuous transformation induced by the variations in the near-surface prevailing winds. In general, ergs have two scales of geometrical roughness, i.e., large-scale dunes and small-scale surface ripples that are spatially periodic [2]–[5]. Previous studies show that the microwave scattering from sand is dominated by surface scattering and is modulated by the sand bedform characteristics [6]–[8].

Microwave emission is a function of surface thermal and geometrical characteristics, and spaceborne radiometric temperature measurements have been used to classify different land surface types [9]–[13]. Azimuthal anisotropy of radiometric temperature has also been investigated. Yu [14] reported directional radiometric temperature variations caused by canopy geometry and row structure in cultivated maize fields. Prigent

et al. [15] reported insignificant azimuth angle dependence over dry sand surface whereas Macelloni *et al.* [16] combined spaceborne radiometric temperature and backscatter measurements to study soil and vegetation. Some investigators have shown that there is strong azimuth angle modulation of microwave emission over the Antarctic surface caused by surface geometry [17]. This research shows that there is significant azimuth angle modulation over sand surfaces caused by sand bedform features.

Ergs have very low moisture content and have a homogeneous, temporally stable distribution of dielectric constant. Thus, temporal variabilities of scattering and emission from sand are mainly a function of geometrical characteristics. Emission also has an additional dependence upon the thermal characteristics of sand. Passive microwave sensors (radiometers) observe the radiometric temperature (T_b) of a target as a measure of its radiometric emission. The T_b value observed is a function of the surface physical temperature and surface emissivity. Over a rough surface, T_b measurements are modulated by the look direction and also depend upon the frequency and polarization of the instrument.

We use dual-polarization T_b measurements at 19 and 37 GHz from the Special Sensor Microwave Imager (SSM/I) aboard the Defense Meteorological Satellite Program (DMSP) [18], [19] and the Tropical Rainfall Measuring Mission (TRMM) Microwave Imager (TMI) [20] and simple electromagnetic models to study the radiometric response of erg surfaces. We introduce an observational empirical model that combines SSM/I and TMI data to estimate the T_b azimuthal anisotropy over sand surfaces. It is shown that the observed T_b is modulated by the look direction and that the modulation is a function of the surface profile. The modulation indicates the surface characteristics, i.e., dune types and their orientation. Shadowing and Sun illumination effects are ignored in explaining the radiometric behavior of sand.

Sand radiometric emission is described in Section II along with a simple facet model to explain the dual-polarization emission over sand dunes. Section II also includes the model simulation of T_b azimuth angle (ϕ) modulation over simple dunes. The ϕ-modulation and time-of-day (t_d) modulation of the observed T_b data and a comparison to model simulation results are given in Section III. This section also compares the T_b observations at 19- and 37-GHz frequencies. A summary and conclusion follows in Section IV.

Three erg sites that have flat sand sheets, transverse dunes, and longitudinal dunes located at 31.7°N, 0.5°E (location 1), 17.5°N, 9.3°W (location 2), and 17.5°N, 15.35°W (location 3), respectively, are selected to study the T_b response. The description of these dune types is given in [6]. The site information is extracted from [21].

II. RADIOMETRIC EMISSION FROM SAND

In this section, a theoretical background of radiometric emission over sand is described. An emission model from layered media is applied to sand in Section II-A, followed by a description of a simple rough facet model of radiometric temperature in Section II-B. Section II-C presents the simulation of the model over simple dune shapes.

A. Background

Sand emission depends upon the desert surface geometry and volumetric dielectric and thermal characteristics. Mathematically, T_b is given by

$$T_b(\theta, \phi; f, p) = e(\theta, \phi; f, p)\mathbf{T}, \qquad p = v, h \qquad (1)$$

where θ and ϕ are the incidence and azimuth angles of observation, respectively, while f, p, $\mathbf{T}$, and e denote the frequency, polarization, physical temperature, and emissivity, respectively. v and h denote vertical (V-pol) and horizontal (H-pol) polarizations, respectively. For very dry soil, the electromagnetic wave penetration depth (δ_p) is approximately equal to its free-space wavelength [15], [22]. The depth of sand that contributes to the measured T_b is called sampling depth (τ) and is related to the penetration depth by $\tau \approx 3\delta_p \cos\theta$ [22]. For soils in the deserts, microwave radiation is estimated to come from soil layers down to depths of five wavelengths and at frequencies greater than 15 GHz, emission is proportional to surface skin temperature [15].

The total emission is the sum of volume and surface emissions. Volumetric emission is nearly isotropic and unpolarized. The air–sand boundary transmission coefficient for V-pol and H-pol polarizations depends on θ, resulting in θ-dependence of T_b. Furthermore, local incidence angle (θ') of tilted dune facets changes with azimuth angle, resulting in ϕ-dependence of T_b. T_b observed by the radiometer is a result of volumetric emission of the sand, modulated by the look direction due to the local surface slope variations.

We use the radiometric emission model for a layered dielectric material given in [23, eqs. 5.2.36a and 5.2.36b]. This model is based on the fluctuating electromagnetic field theory of dissipative materials. The electromagnetic field is produced by the spontaneous local electric and magnetic moments arising from the thermally induced random motion of its charges. This model is derived for a stratified material with a temperature profile. The medium has $n + 1$ layers where the $(n + 1)$th layer extends infinitely below the nth layer. $\mathbf{T}_l$ and ϵ_l denote the physical temperature and electrical permittivity of the lth layer, respectively, and d_{l-1} and d_l denote the distance of the layer's upper and lower boundaries, respectively, from the air–sand boundary. In the model, the sampling depth is divided into n layers with the $(n + 1)$th layer being the remaining half space of sand below sampling depth. Thus, the distance of the lower boundary of the nth layer is equal to the sampling depth, i.e., $d_n = \tau$.

Sand is a spatially homogeneous medium. We model it as an infinite half space with isothermal horizontal strata and a smooth vertical temperature profile. Since sand in the Sahara desert has a low moisture content that does not change over time, we assume the sand to have a temporally stable dielectric constant. Moreover, we assume the sand dielectric constant to be spatially homogeneous within the footprint of observation. The vertical temperature profile of sand depends on time-of-day and season

(time-of-year). During the day time, the sand surface temperature is higher than the subsurface temperature, and lower at night. We apply a mean diurnal temperature profile to the model and assume it falls off exponentially from a surface temperature (T_0) to a nominal subsurface temperature (T_τ) over the sampling depth τ. After applying these considerations, the radiometric temperature for H-pol (T_{bh}) and V-pol (T_{bv}) given in [23] becomes

$$T_{bh}(\theta) = \frac{k_0}{\cos\theta}\frac{\epsilon_1''}{\epsilon_0}\left|T_{01}^{TE}\right|^2$$
$$\times \left[\mathbf{T}_t e^{-2k_{1z}''d_n} - \sum_{l=1}^{n}\left\{\mathbf{T}_l\left(e^{-2k_{1z}''d_l} - e^{-2k_{1z}''d_{l-1}}\right)\right\}\right]$$

$$T_{bv}(\theta) = \frac{k_0}{\cos\theta}\frac{\epsilon_1''}{\epsilon_0}\left(\frac{|k_{1z}|^2 + k_x^2}{|k_1|^2}\right)\left|\frac{k_0}{k_1}T_{01}^{TM}\right|^2$$
$$\times \left[\mathbf{T}_t e^{-2k_{1z}''d_n} - \sum_{l=1}^{n}\left\{\mathbf{T}_l\left(e^{-2k_{1z}''d_l} - e^{-2k_{1z}''d_{l-1}}\right)\right\}\right]$$
$$(2)$$

where k_0, θ, and ϵ_0 are the wavenumber, incidence angle, and electrical permittivity in the air, respectively. k_1 and k_{1z} are the wavenumber and its z component in the sand, respectively. ϵ_1'' and k_{1z}'' denote the imaginary parts of complex electrical permittivity and k_{1z} in sand, respectively. $k_x = k_0 \sin\theta$ is the surface component of incident wavenumber. T_{01}^{TE} and T_{01}^{TM} denote the transmission coefficients between air and sand for H- and V-pol, respectively. $\mathbf{T}_l$ and $\mathbf{T}_t$ are the physical temperatures of lth and $(n+1)$th layer, respectively. In the derivation of (2), Tsang [23] has taken into account the effect of reflections between layers.

Dry sand has a low relative electrical permittivity (ϵ_r) and we use a nominal value of $2 + i10^{-4}$ in the simulation of (2) [24]. The corresponding Brewster angle is approximately 55°. The diurnal mean surface and subsurface temperatures are assumed to be 330 and 310 K with a sampling depth of 6 cm (about four wavelengths at 19 GHz) and $n = 100$ (101 layers). Fig. 1(a) shows θ-response of both T_{bh} and T_{bv} computed from (2). At nadir, V-pol and H-pol T_b have the same value and T_{bh} decreases as θ is increased. On the other hand, T_{bv} increases initially and reaches its maximum at the Brewster angle beyond which it rapidly rolls-off. T_{bv} is higher than T_{bh} for off-nadir incident directions and the difference between two radiometric temperatures is also a function of θ. We define the polarization difference (ΔT_b) as

$$\Delta T_b(\theta, \phi) = T_{bv}(\theta, \phi) - T_{bh}(\theta, \phi). \qquad (3)$$

The local incidence angle θ' is a function of look direction (θ, ϕ) and surface tilt (θ_s, ϕ_s) where θ_s and ϕ_s are the spherical angles of the facet's unit normal. Since SSM/I and TMI observations are made at fixed $\theta = 53°$, for a fixed azimuth direction ϕ the local incidence angle θ' depends only on (θ_s, ϕ_s). Thus, ΔT_b is a function of tilt of the surface. This also makes the polarization of the emitted wave a function of the surface tilt, i.e., a wave from a tilted surface has a different polarization than from a flat surface. Fig. 1(a) also shows the incidence angle dependence of ΔT_b, which gradually increases with θ (ΔT_b is zero at nadir), and decreases rapidly back to zero at grazing incidence angles. Plots 1(b)–(f) illustrate the sensitivity of T_b and ΔT_b to other model parameters. The responses have insignificant dependence on surface temperature [Fig. 1(b)] and sampling depth
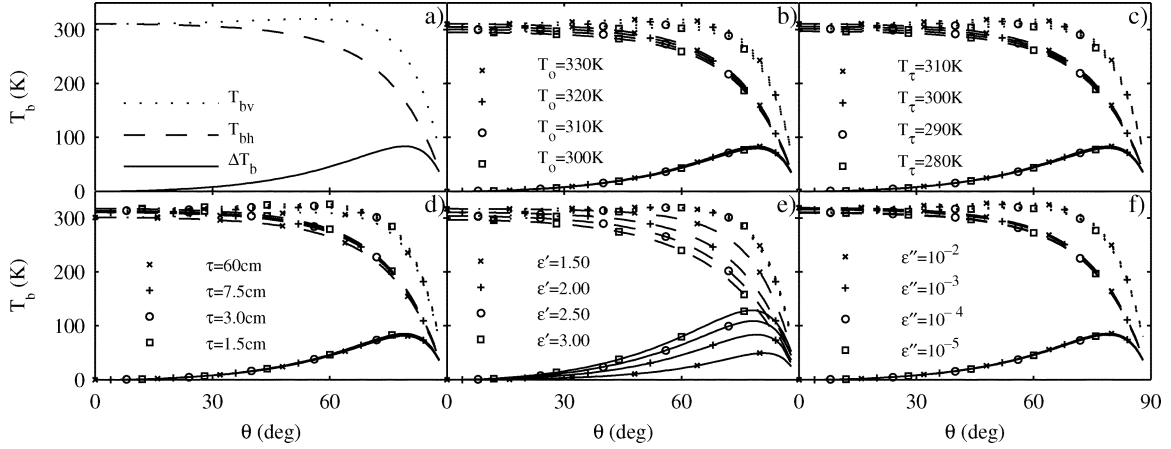
Fig. 1. (a) T_b and ΔT_b model simulations for $T_0 = 330$ K, $T_\tau = 310$ K, and $\tau = 6$ cm when a radiometer observes sand material with $\epsilon_r = 2 + i10^{-4}$ at 19-GHz frequency. (b)–(d) Changes in plot (a) due to variations in model parameters. (b) and (c) Dependence on surface and subsurface nominal temperature, respectively. (d) Variations with sampling depth. (e) and (f) Dependence on the real and imaginary parts of relative electrical permittivity of the material, respectively.

[Fig. 1(d)]. Subsurface nominal temperature [Fig. 1(c)] and the imaginary part of complex electrical permittivity [Fig. 1(f)] alter the T_b response but do not have significant effect on ΔT_b. The real part of complex electrical permittivity has the most significant effect on ΔT_b [Fig. 1(e)]. This analysis demonstrates that ΔT_b mainly depends on the real part of ϵ_r and, for practical purposes, is insensitive to other model parameters. This makes ΔT_b very suitable for modeling the ϕ response over the sand dune bedforms.

B. Facet Model

An erg is composed of large-scale dunes that are modeled as rough facets with a tilt distribution [6], [22]. Each rough facet is characterized by a tilt distribution $P(\theta_s, \phi_s)$, which is the probability of occurrence of a local unit normal in the (θ_s, ϕ_s) direction. We model T_b from a tilted facet (denoted by T_{bf}) is the weighted average of T_b from all parts of the facet where the probability distribution of tilt is used as the weighting function. T_{bf} as a function of look direction (θ, ϕ) and polarization p is given by

$$T_{bf}(\theta, \phi; p) = \int T_b(\theta'; p, T_o, T_\tau, \tau)P(\theta_s, \phi_s)d\theta' \quad (4)$$

where θ' is the local incidence angle, which is a function of the surface tilt (θ_s, ϕ_s) and radiometer's look direction (θ, ϕ). $T_b(\theta'; p, T_o, T_\tau, \tau)$ is the radiometric response of a flat facet (with zero tilt) as given in Fig. 1(a). A zero-tilt facet is azimuthally isotropic, i.e., $T_b(\theta, \phi) = T_b(\theta)$ and $\theta' = \theta$; thus, any azimuthal anisotropy results from the nonzero tilt of the facet surface. ΔT_b of a facet is given by

$$\Delta T_{bf}(\theta, \phi) = \int \Delta T_b(\theta')P(\theta_s, \phi_s)d\theta'. \quad (5)$$

Note that dependence on polarization and thermal characteristics is dropped since ΔT_b is independent of these characteristics.

The response of the dunes is the linear combination of the responses from the individual dominant facets weighted by their projected area. Thus, we model the total radiometric response from dunes (denoted T_{bd}) at p-polarization to be

$$T_{bd}(\theta, \phi; p) = \frac{1}{A'} \sum_n A'_n \int T_b(\theta'; p, T_o, T_\tau, \tau)P_n(\theta_s, \phi_s)d\theta' \quad (6)$$
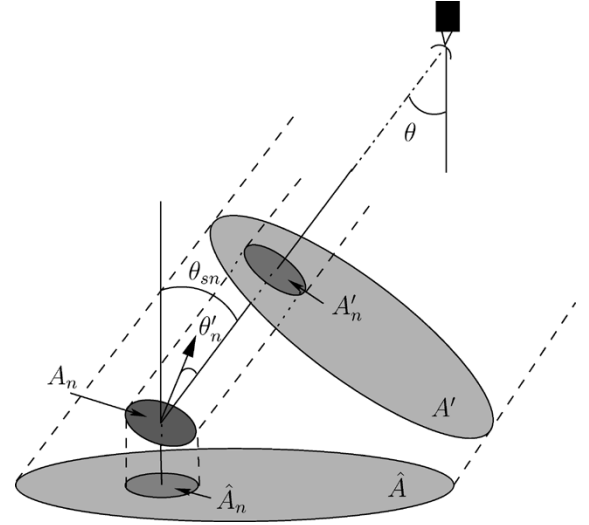

Fig. 2. Area of facet projection onto antenna beam cross section and ground surface.

where A' and A'_n are the projected areas of the antenna foot print and nth rough facet, respectively (Fig. 2). The summation is over all the dominant rough facets in the footprint of the sensor. If $\hat{A}$ is the surface area illuminated at an incidence angle θ, and A_n is the actual surface area of the facet with a local incidence angle θ'_n, then $A' = \hat{A}\cos\theta$ and $A'_n = A_n\cos\theta'_n$. The tilt angle θ_{sn} of the facet is related to its horizontal projection $(\hat{A}_n)$ by $\hat{A}_n = A_n\cos\theta_{sn}$. Using these relationships in (6) we obtain

$$T_{bd}(\theta, \phi; p) = \sum_n \frac{F_n \cos\theta'_n}{\cos\theta_{sn}\cos\theta}$$

$$\times \int T_b(\theta'; p, T_o, T_\tau, \tau)P_n(\theta_s, \phi_s)d\theta'$$

$$F_n = \frac{\hat{A}_n}{\hat{A}} \quad (7)$$

where F_n is the fraction of footprint area covered by the nth facet that has a mean tilt angle θ_{sn} and a mean local incidence
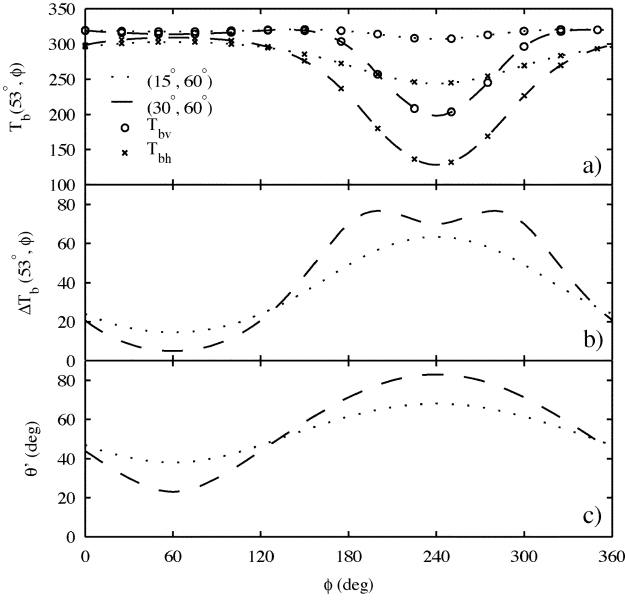
Fig. 3. Computed (a) T_b and (b) ΔT_b ϕ-response over two different facets with Gaussian tilt distribution. (c) Plots corresponding θ' variations with ϕ.
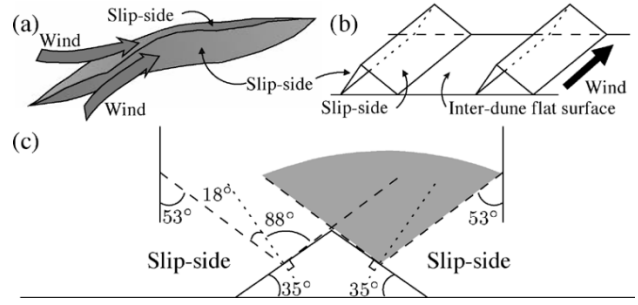

Fig. 4. (a) Longitudinal dune, (b) its three-facet model, and (c) cross section of a typical dune. The shaded portion is the projection of the cone of view formed by all view azimuth angles. The cone represents the range of local incidence angles for the given tilt.

angle θ'_n. F_n is related to the dune shape and is easily estimated for simple dunes. The net ΔT_b over the dune field is given by

$$\Delta T_{bd}(\theta, \phi) = \sum_n \frac{F_n \cos \theta'_n}{\cos \theta_{sn} \cos \theta} \int \Delta T_b(\theta') P_n(\theta_s, \phi_s) d\theta'. \quad (8)$$

C. ΔT_b Response Over Model Dunes

In this section we use the rough facet model [(7), (8)] to determine the simulated T_b and ΔT_b response over simple dune surfaces. First, the simulation results over single tilted facets are presented. The facet radiometric response model [(4), (5)] is applied separately to two different facets tilted at $15°$ and $30°$ that correspond to the wind- and slip-side slopes of a transverse dune. The azimuth orientation ϕ_s of the facets is $60°$. The α-angle is defined as the sensor azimuth angle relative to the facet azimuth orientation given by $\alpha = \phi - \phi_s$. Fig. 3 shows the ϕ-response of simulation results at a sensor incidence angle of $53°$ (corresponding to the incidence angle of SSM/I and TMI). The magnitude of H- and V-pol T_b ϕ-modulation increases with the slope of the facet and minimum T_b occurs when $\alpha = 180°$. T_{bv} is higher than T_{bh}, and the difference ΔT_b is minimum at $\alpha = 0°$ [Fig. 3(b)] since θ' is minimum at this α-angle [Fig. 3(c)]. The maximum of ΔT_b and θ' occur at $\alpha = 180°$. For steeper facets, θ' approaches grazing angles at $\alpha = 180°$, resulting in a drop of ΔT_b at the facet grazing angle [Fig. 1(a)].

The T_b ϕ-response of a tilted facet depends upon the slope and azimuth orientation of the facet: T_b is inversely proportional to the local incidence angle, T_{bv} and T_{bh} have distinct ϕ-responses, and T_{bv} is higher in magnitude than T_{bh}. ΔT_b is directly proportional to θ'. The minima and maxima of ΔT_b ϕ-modulation over tilted facets correspond to α-angles of $0°$ and $180°$, respectively. In the next two subsections, the results of the simulation over model longitudinal and transverse dunes are presented.

1) Longitudinal Dunes: A longitudinal dune is characterized by two slip sides and a flat interdune area as shown in Fig. 4

[6]. The slope of both slip-sides is $30°$ to $35°$ (the angle of repose of sand) and their azimuth orientations differ by $180°$. The long axis of the dune is $90°$ relative to the azimuth directions of the slip-sides and is along the mean wind direction that formed the dune. We model the longitudinal dune as a composite of three rough facets that correspond to two slip-sides and an interdune flat surface. The cross section of a longitudinal dune shown in Fig. 4(c) indicates the minimum and maximum local incidence angles resulting from the slopes of the facets as viewed by a sensor at an incidence angle of $53°$. As ϕ changes, θ' of the facet changes between the minimum and maximum values. In the model simulation, the two slip-sides have a Gaussian tilt distribution for (θ_s, ϕ_s) with means $(30°, 170°)$ and $(30°, 350°)$ and standard deviations of $5°$ each. The covariance between θ_s and ϕ_s is assumed to be zero in this research. The flat interdune facet has a mean tilt of $(0°, 0°)$ with a standard deviation of $(5°, 10°)$ and zero covariance. Fig. 5 shows the model T_b and ΔT_b results. The two slip-sides of the longitudinal dune result in two maxima in T_{bh}, and two minima in T_{bv} ϕ-responses. The ϕ angle at which these maxima or minima occur correspond to the azimuth directions of the facets. This opposite behavior of T_{bv} and T_{bh} results in minimum ΔT_b when ϕ is along the azimuth directions of the slip-sides. ΔT_b is minimum when a slip-side has a near nadir view and increases when ϕ is changed from this direction. Simultaneously, the contribution from the other slip-side starts increasing and this results in an azimuth modulation signal in ΔT_b with peaks occurring when ϕ is along the axis of the dune. ΔT_b is maximum at ϕ directions along the axis of the dune.

2) Transverse Dunes: A transverse dune has a wind-side slope of $10°$ to $15°$ and a slip-side slope similar to a longitudinal dune. The azimuth directions of these two sides differ by $180°$. The axis of the dune is defined similar to a longitudinal dune, but the wind direction that produces this dune corresponds to the azimuth direction of the slip-side, i.e., perpendicular to the long axis of the dune. We model the transverse dune as a composite of three rough facets that correspond to a slip-side, a wind-side, and an interdune flat surface [6]. Fig. 6(b) illustrates the three-facet model for a transverse dune. Fig. 6(c) shows the cross section of a transverse dune where the shaded portion represents the range of possible local incidence angles for each facet viewed at $\theta = 53°$.

Interdune flat facet, wind-side, and slip-side are assumed to have Gaussian tilt distributions for (θ_s, ϕ_s) with means $(0°, 0°)$,
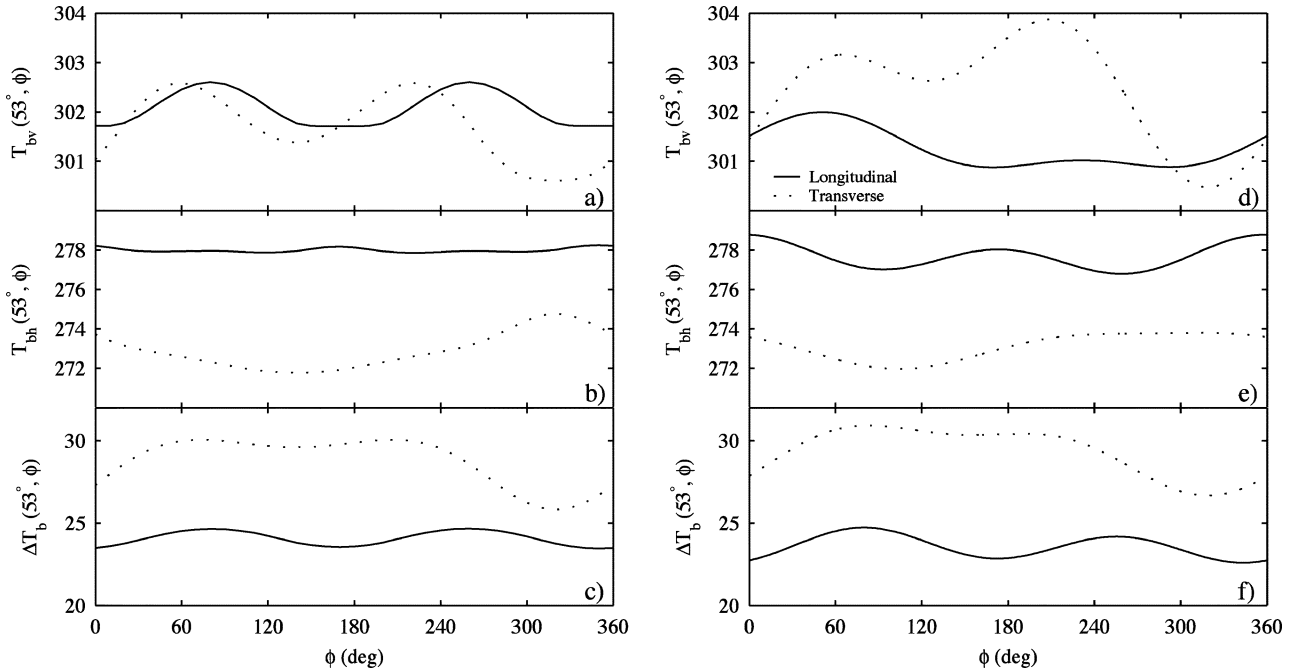
Fig. 5. (a)–(c) Simulated T_b and ΔT_b responses over triple-facet transverse and longitudinal dune models. (d)–(f) T_b and ΔT_b responses derived from SSM/I and TMI observed data at 19 GHz (see text).
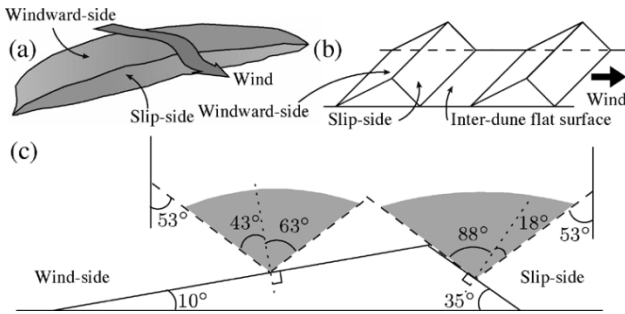

Fig. 6. (a) Transverse dune, (b) its three-facet model, and (c) cross section. The shaded portion is the projection of the cone of view formed by all view azimuth angles. The cone represents the range of local incidence angles for the given tilt.

$(12°, 50°)$, and $(30°, 230°)$, respectively, and standard deviations $(3°, 5°)$, $(3°, 10°)$, and $(3°, 10°)$, respectively. The covariance between θ_s and ϕ_s is zero. Fig. 5 shows the model results for a transverse dune. The T_b ϕ-response is similar to longitudinal dunes, but has a higher magnitude of modulation. In the ΔT_b response, the global minimum in the ϕ modulation occurs in the azimuth direction of the slip-side of the dune whereas a second minimum occurs at the wind-side azimuth direction. Fig. 5(d) and (e) summarizes the ϕ-modulation of the observed data described in Section III.

The analysis of model simulations over individual facets and composite facet surfaces suggests that T_{bv} and T_{bh} have significant ϕ-modulation caused by the tilted rough surfaces. Since ΔT_b is independent of the thermal characteristics of the surface, its ϕ-modulation is only dependent upon the dielectric constant and surface geometrical characteristics. Model simulations at 37 GHz give similar ϕ-modulation with a lower mean value due to higher attenuation. The ΔT_b ϕ-modulation of model dune surfaces reflects the presence of tilted facets and helps identify the underlying dune types.

III. SPACEBORNE T_b OBSERVATIONS

In this section, dual-polarization 19- and 37-GHz T_b measurements from TMI and SSM/I over Saharan ergs are used to analyze the radiometric emission behavior of dunes in comparison with model prediction. TMI and SSM/I make T_b measurements at an incidence angle of 52.75° and 53.4°, respectively. The scan pattern of TMI and SSM/I sensors, in combination with the orbit geometry of the ascending and descending passes, provides T_b measurements sampled at many azimuth angles.

The orbit of the TRMM satellite is inclined at approximately 30°. The orbit longitude of the ascending node shifts every repeat cycle. This helps TMI acquire T_b measurements of the target sampled at various times-of-day. SSM/I acquisition of the target is made in a sun-synchronous orbit at two times-of-day. We combine SSM/I data from three DMSP satellites (F13, F14, and F15) to obtain six times-of-day (t_d) samples (see Fig. 9).

Sand in the tropics undergoes a diurnal cycle of temperature variation. The solar incident radiation intensity is a function of time-of-day and season (time-of-year). Illuminated by the Sun during the day, sand absorbs the Sun's radiation, which increases its internal and surface temperature. Sand cools down during the night by dissipating thermal radiation. Fig. 7 shows the resulting diurnal variation of T_{bv} and T_{bh} observed by TMI and SSM/I sensors. The data is acquired during Julian day (JD) 185-2002 and JD 238-2002 and is shown for three erg targets: flat sand sheet, transverse dunes, and longitudinal dunes. The two sensors show good cross-calibration and similar diurnal modulation. ΔT_b is also plotted and reveals higher noise over the dunes (compared to sand sheet) due to the higher ϕ-modulation caused by dune surface geometry. The small variation of T_b over the sand sheet indicates insignificant ϕ-modulation.

As previously noted, ΔT_b is dependent on the surface profile characteristics and dielectric constant. The local incidence angle over a flat sand sheet [Fig. 7(d)] is almost equal to the incidence angle of observation $(\theta' = 53°)$ and does not change with the
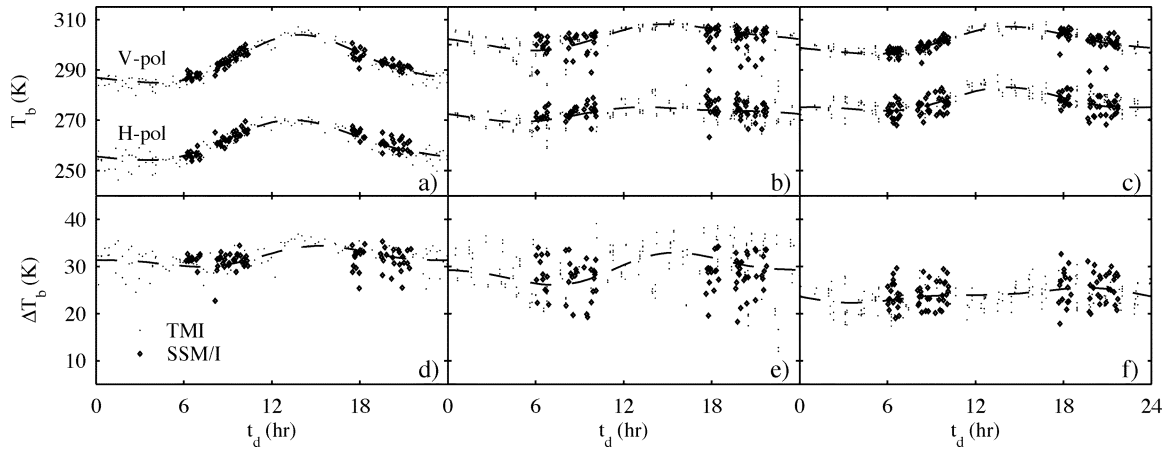
Fig. 7. Dual-polarization 19-GHz T_b diurnal modulation from TMI and SSM/I over (a) a flat sand sheet, (b) transverse dunes, and (c) longitudinal dunes. Corresponding polarization difference is plotted in (d), (e), and (f), respectively. The dashed line represents a second-order harmonic fit through the radiometric temperature measurements as a function of time-of-day t_d.
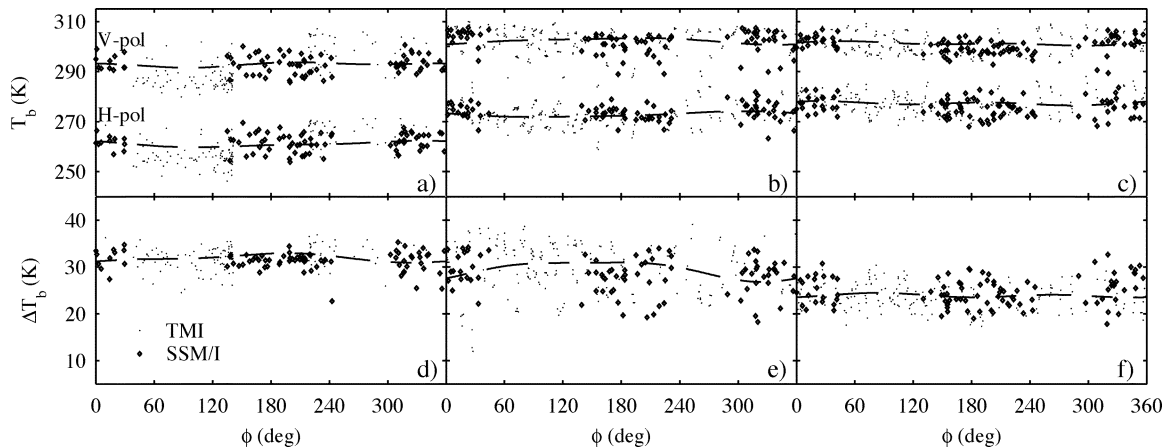

Fig. 8. Dual-polarization 19-GHz T_b azimuth angle modulation from TMI and SSM/I over (a) a flat sand sheet, (b) transverse dunes, and (c) longitudinal dunes. Corresponding polarization difference is plotted in (d), (e), and (f), respectively. The dashed line represents a second-order harmonic fit through the radiometric temperature measurements as a function of ϕ.

azimuth angle resulting in a ΔT_b of about 30 K (Fig. 1). Over transverse dunes [Fig. 7(e)] the tilt of wind- and slip-sides results in more contribution at relatively smaller local incidence angles, thus reducing ΔT_b. Over the slip-side, the minimum θ' is 18° (Fig. 4). This is also evident from the longitudinal dunes [Fig. 7(f)] where ΔT_b is further reduced due to the presence of two slip-sides. It should also be noticed that ΔT_b also has a minor diurnal variation. The azimuth angle sampling of the data contributes to ΔT_b diurnal variation. The diurnal variation of the surface emissivity and surface small-scale features (ripples) and Sun inclination also contribute to ΔT_b diurnal variation. This t_d-response is well modeled by a second-order harmonic equation shown with dashed lines.

Fig. 8 depicts the azimuth angle variation of observed T_b. The magnitude of the azimuth angle modulation is lower than the diurnal modulation but reveals useful information about the surface bedform characteristics. Combining the data from two sensors results in a denser azimuth angle sampling. The high variance in the data is due to sampling of data at different times-of-day. The analysis of the T_b azimuth angle variation at a narrow range of t_d reveals that T_b ϕ-modulation also follows a second-order harmonic relationship shown with dashed lines.
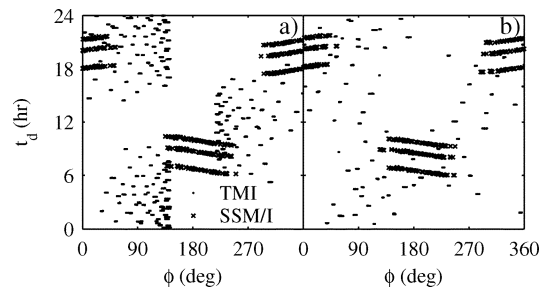
Fig. 9. $\phi - t_d$ sampling of data from combined TMI and SSM/I data over (a) location 1 and (b) location 2 during JD 185-2002 and JD 238-2002.

The T_b observations have coupled dependence on the t_d and ϕ. The magnitude of azimuth modulation is very low compared to the magnitude of the diurnal variation. Based on the observed ϕ- and t_d-modulation of both T_b and ΔT_b, a descriptive empirical observation model is used to remove the t_d dependence of the data. We use a simple additive model given by

$$\Delta T_b(t_d, \phi) = T_{bm} + \mathcal{T}_t(t_d) + \mathcal{T}_\phi(\phi) \qquad (9)$$

Fig. 10.   Surface of the model fit given in (9) for a longitudinal dune field. Slices through the model fit at fixed ϕ values (left) and fixed t_d values (right) are shown. (a)–(c) 19-GHz T_{bv} surface model fit, slices through fixed ϕ values, and slices through fixed t_d values, respectively. (d)–(f)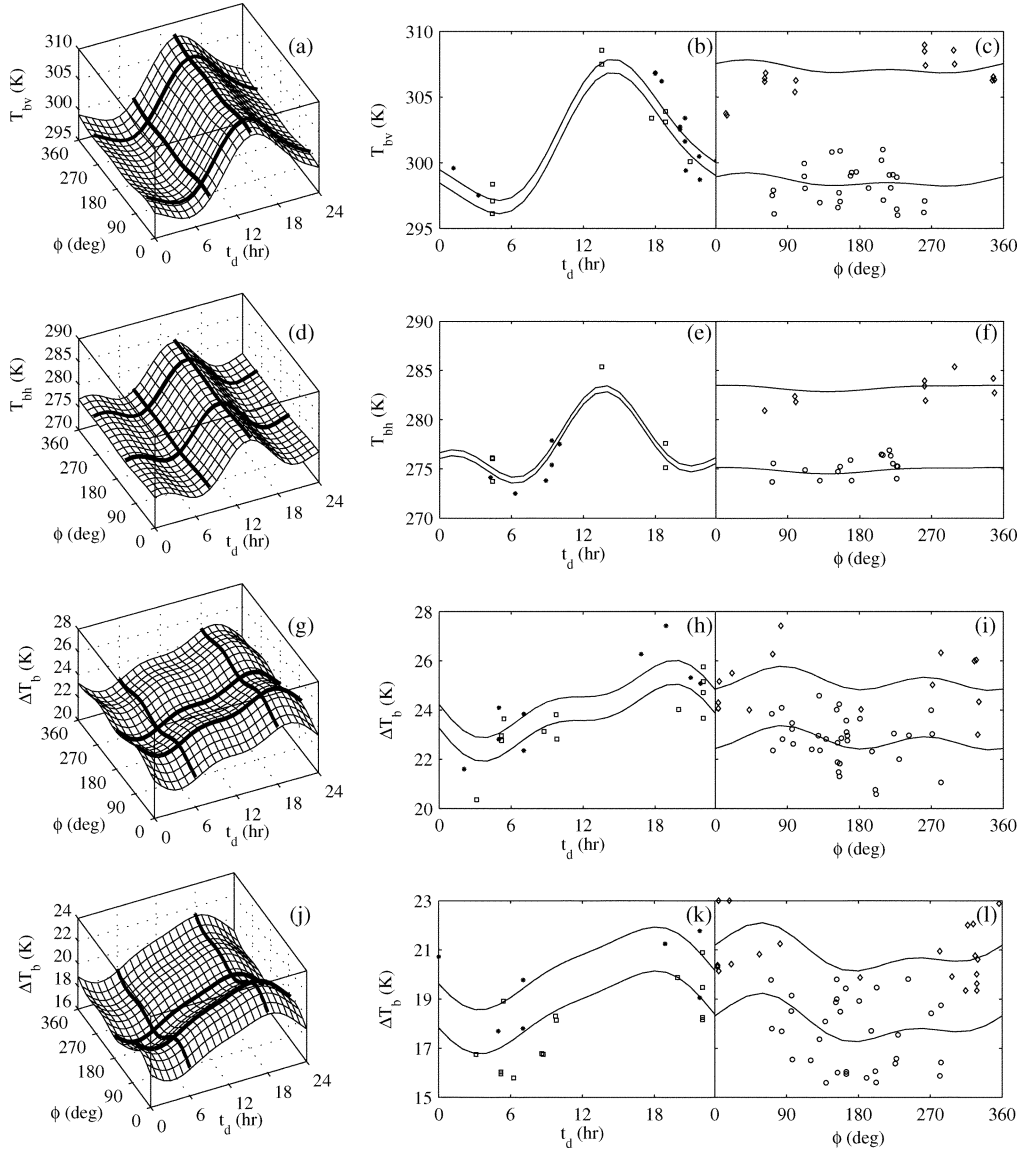 19-GHz T_{bh} surface model fit, slices through fixed ϕ values, and slices through fixed t_d values, respectively. (g)–(i) 19-GHz ΔT_b surface model fit, slices through fixed ϕ values, and slices through fixed t_d values, respectively. (j)–(l) 37-GHz ΔT_b surface model fit, slices through fixed ϕ values, and slices through fixed t_d values, respectively.

$$\mathcal{T}_t(t_d) = N_1 \cos\left(\frac{\pi}{12}(t_d - t_{d1})\right) + N_2 \cos\left(\frac{\pi}{12}(2t_d - t_{d2})\right)$$
$$\mathcal{T}_\phi(\phi) = M_1 \cos(\phi - \phi_1) + M_2 \cos(2\phi - \phi_2) \quad (10)$$

where T_{bm} is the mean polarization difference. $\mathcal{T}_t(t_d)$ and $\mathcal{T}_\phi(\phi)$ model the t_d and ϕ dependence of the polarization difference, respectively. In this model the nominal radiometric temperature T_{bm} is modulated by two second-order harmonics caused by the time-of-day and the azimuth angle of observation. We apply this empirical model to the data and perform a surface fit to the data using a least squares solution. The accuracy of the fit to this model depends upon the $\phi - t_d$ sampling of the data. ϕ-modulation after removal of t_d dependence from observations is consistent with the theoretical model used in Section II. Fig. 9 shows the $\phi - t_d$ sampling of the combined TMI and SSM/I data over two target areas. Although the sampling is irregular, sparse, and contains large gaps, the least squares fit provides a reasonable estimate of the model parameters. Using both TMI and SSM/I data improves the ϕ-sampling of

observations. T_{bv} and T_{bh} dependence on t_d and ϕ is also modeled by a sum of two second-order harmonics.

Fig. 10 illustrates the surface fit to the 19-GHz observed data and slices at particular ϕ and t_d. The solid lines correspond to slices through the surface at different t_d and ϕ as shown on the right side of the surface fit plots. The slice plots also show actual observations selected within $t_d = \pm 2$ h and $\phi = \pm 15°$ around the t_d and ϕ values of slice, respectively. Fig. 10(j)–(l) shows the ΔT_b surface fit and slices for 37 GHz. T_{bv} and T_{bh} surface fits for 37 GHz are similar to 19 GHz with different mean T_b. The model parameters of the surface fits are shown in Table I. We use the model fit parameters to remove the t_d dependence of T_b and ΔT_b to retrieve the ϕ-modulation of the data shown in Fig. 5(d)–(f). The plots from the model and observations show similar results for both types of dunes. The comparison confirms that the presence of tilted facets modulates the radiometric temperature of the sand surface. Although the mean values of T_{bv} and T_{bh} for the model simulation are slightly

TABLE I
TABLE LISTING THE PARAMETERS OF MODEL (9) FIT TO OBSERVED
DATA OVER TRANSVERSE DUNE AT 19 AND 37 GHz

	A	N_1	t_{d1}	N_2	t_{d2}	M_1	ϕ_1	M_2	ϕ_2
T_{bv} 19 GHz	301.31	5.04	-2.29	1.15	0.77	0.37	0.70	0.28	1.31
T_{bh} 19 GHz	277.52	3.33	-2.55	2.46	0.81	0.31	-0.63	0.11	1.62
ΔT_b 19 GHz	23.88	1.22	-1.7	0.60	-1.73	0.23	1.51	0.37	2.90
T_{bv} 37 GHz	296.82	6.34	-2.42	1.61	0.71	0.53	0.49	0.18	1.02
T_{bh} 37 GHz	277.37	4.74	-2.61	2.24	0.68	0.29	-1.08	0.15	3.09
ΔT_b 37 GHz	19.35	1.55	-1.96	0.37	-1.96	0.75	0.81	0.45	2.21

TABLE II
TABLE LISTING RMS ERRORS FOR DIFFERENT MODELS AND CASES
USED IN THIS RESEARCH. THE STANDARD DEVIATION OF
RAW DATA (STD) IS SHOWN FOR COMPARISON

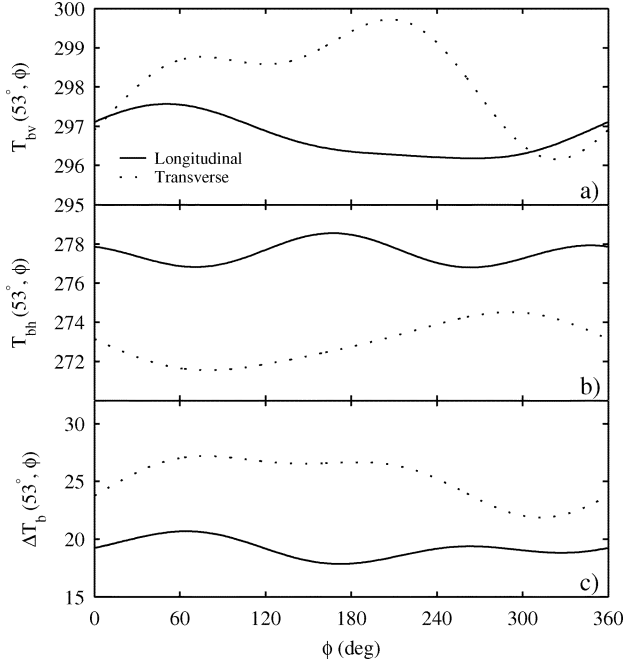| Cases and Frequencies	Std	Empirical Models			Facet model
		t_d	ϕ	t_d & ϕ	
Linear Dune T_{bv} 19 GHz	4.00	1.74	3.49	1.50	4.16
Linear Dune T_{bh} 19 GHz	4.18	2.96	3.83	2.74	4.22
Linear Dune ΔT_b 19 GHz	2.70	2.44	2.55	2.41	2.66
Transverse Dune T_{bv} 19 GHz	5.85	4.44	5.59	4.33	5.92
Transverse Dune T_{bh} 19 GHz	4.19	3.50	3.80	3.36	3.97
Transverse Dune ΔT_b 19 GHz	5.22	4.95	5.17	4.83	5.31
Linear Dune T_{bv} 37 GHz	4.95	2.01	4.38	1.64	12.01
Linear Dune T_{bh} 37 GHz	4.71	3.16	4.46	2.90	7.39
Linear Dune ΔT_b 37 GHz	3.13	2.70	2.83	2.63	6.07
Transverse Dune T_{bv} 37 GHz	6.17	4.48	5.86	4.30	11.20
Transverse Dune T_{bh} 37 GHz	4.66	4.07	4.29	3.96	6.74
Transverse Dune ΔT_b 37 GHz	6.92	6.51	6.82	6.32	8.16

Fig. 11. (a)–(c) simulated T_b and ΔT_b response over triple-facet transverse and longitudinal dune models. (d)–(f) T_b and ΔT_b response derived from SSM/I and TMI observed data at 37 GHz.

The results reveal the dominant effect of surface geometry and are similar to those found from model simulations. The simulated and observed ΔT_b reveal significant similarity in magnitudes and phases. The difference in T_{bv} and T_{bh} between the model simulation and the observed data may be due to ignoring the Sun inclination and because the subsurface temperature profile used does not represent the actual sand thermal conditions.

IV. SUMMARY AND CONCLUSION

Radiometric emissions from erg surfaces are analyzed using SSM/I and TMI dual-polarization T_b observations. Combining the data from the two sensors improves the azimuth angle sampling of the data. The observed T_b versus ϕ is modulated by the surface geometrical characteristics and reflects the presence of dominant dune facets. ΔT_b has negligible dependence on the thermal characteristics of the surface and its ϕ-modulation varies with changes in the surface geometrical characteristics.

A simple rough facet model is used to model the T_b response from the erg surface. Large-scale dunes are treated as composed of dominant facets. An emission model based on fluctuating electromagnetic field theory for dissipative materials is used to estimate the T_b and ΔT_b incidence angle response for a flat sand surface. The total T_b from dunes is the weighted sum of T_b response from its dominant facets. When modeled as surfaces composed of multiple rough facets, longitudinal and transverse dunes exhibit significant differences in their T_b and ΔT_b ϕ-modulation: ΔT_b decreases whereas T_b increases due to a decrease in θ'. Thus, a tilted facet reveals its presence as a minimum in ΔT_b ϕ-response, where the magnitude of the ΔT_b reflects the tilt of the facet. The model simulation results are consistent with the satellite observations over areas of known dune types. Model simulation and satellite observations at 19 and 37 GHz provide similar information about the dune shape and type.

TMI-acquired T_b observations at many times-of-day reveal the diurnal temperature cycle of the sand surface. The time-of-day dependence is removed by using a descriptive empirical observation model with two additive second-order

different from the observations, the modulation characteristics are similar. In the case of ΔT_b, both the mean and the magnitude of the ϕ-modulation are consistent between the model and the observations. Fig. 11 shows similar ϕ-modulation from observations at 37 GHz. The mean T_b and ΔT_b are lower than 19 GHz due to higher attenuation. Table II lists the root mean square (rms) errors of different model fits used. RMS error is the square root of the mean of the squared differences between the model and the observations. The additive (t_d, ϕ) second-order harmonic model reduces the rms error of fit compared to the individual second-order harmonic fits for t_d and ϕ. The facet model of layered sand has higher rms error than the observation model; however, all the models fit better to the ΔT_b. Given the uncertainties in the assumptions used in the facet model, it is remarkably accurate. The fits have higher error over transverse dune area due to higher surface profile variations than the longitudinal dune area. Moreover, the rms error increases with frequency. The correlation coefficients between facet model and empirical observation model fit for T_{bv}, T_{bh}, and ΔT_b of longitudinal dunes are 0.22, 0.79, and 0.95, respectively, and 0.60, 0.91, and 0.95, for transverse dunes.

harmonics. Although there is significant T_b diurnal dependence, it is shown that T_b ϕ-modulation of 2–5 K is observed as a result of surface geometrical characteristics. The ϕ-modulation of ΔT_b depends upon the tilt and orientation of the facets in the footprint of the sensor and can be used to distinguish between longitudinal and transverse dune surfaces. A logical extension of this result is to invert the proposed model to extract surface geometry from the T_b observations. The ϕ-modulation caused by surface geometry is quite significant and needs to be taken into consideration while studying such surfaces or calibrating radiometers over such terrains. The complementarity of passive and active remote sensing can be explored by combining microwave emission and scattering observations over sand surfaces. The analysis can be extended to other surfaces with periodic geometries such as snow for a better understanding of their radiometric emissions. The understanding of radiometric emissions over such surfaces can help in the design of future precision radiometers. We note that this research ignores the shadowing and Sun illumination effects in explaining the radiometric behavior of sand.

REFERENCES

[1] R. G. Kennett and F. K. Li, "Seasat over-land scatterometer data, Part I: Global overview of the Ku-band backscatter coefficients," *IEEE Trans. Geosci. Remote Sens.*, vol. 27, no. 5, pp. 592–605, Sep. 1989.

[2] R. U. Cooke and A. Warren, *Geomorphology of Deserts*. London, U.K.: Anchor, 1973.

[3] A. S. Goudie, I. Livingstone, and S. Stokes, *Aeolian Environments, Sediments and Landforms*. New York: Wiley, 1999.

[4] K. Pye and H. Tsoar, *Aeolian Sand and Sand Dunes*. London, U.K.: Unwin, 1990.

[5] R. A. Bagnold, *The Physics of Blown Sand and Desert Dunes*. London, U.K.: Methuen, 1941.

[6] H. Stephen and D. G. Long, "Analysis of scatterometer observations of Saharan ergs using a simple rough facet model," in *Proc. IGARSS*, vol. 3, 2004, pp. 1534–1537.

[7] ——, "Microwave backscatter modeling of erg surfaces in the Sahara desert," *IEEE Trans. Geosci. Remote Sens.*, vol. 43, no. 2, pp. 238–247, Feb. 2005.

[8] L. Bateson and I. H. Woodhouse, "Observations of scatterometer asymmetry over sand seas and derivation of wind ripple orientation," *Int. J. Remote Sens.*, vol. 25, no. 10, pp. 1805–1816, 2004.

[9] K. F. Kunzi, S. Patil, and H. Rott, "Snow-cover parameters retrieved from Nimbus-7 Scanning Multichannel Microwave Radiometer (SMMR) data," *IEEE Trans. Geosci. Remote Sens.*, vol. GE-20, pp. 452–467, 1982.

[10] R. R. Ferrero, N. C. Grody, and J. A. Kogut, "Classification of geophysical parameters using passive microwave satellite measurements," *IEEE Trans. Geosci. Remote Sens.*, vol. GE-24, pp. 1008–1013, Nov. 1986.

[11] M. J. McFarland, R. L. Miller, and C. M. Neale, "Land-Surface temperature derived from the SSM/I passive microwave brightness temperatures," *IEEE Trans. Geosci. Remote Sens.*, no. 5, pp. 839–845, Sep. 1990.

[12] C. M. U. Neale, M. J. McFarland, and K. Chang, "Land-surface-type classification using microwave brightness temperatures from the Special Sensor Microwave/Imager," *IEEE Trans. Signal Process.*, vol. 28, no. 5, pp. 829–838, Sep. 1990.

[13] J. V. Fiore and N. C. Grody, "Classification of snow cover and precipitation using SSM/I measurements: Case studies," *Int. J. Remote Sens.*, no. 13, pp. 3349–3361, 1992.

[14] T. Yu, X. Gu, G. Tian, M. Legrand, F. Baret, J.-F. Hanocq, R. Bosseno, and Y. Zhang, "Modeling directional brightness temperature over a maize canopy in row structure," *IEEE Trans. Geosci. Remote Sens.*, vol. 42, no. 10, pp. 2290–2304, Oct. 2004.

[15] C. Prigent, W. B. Rossow, E. Matthews, and B. Marticorena, "Microwave radiometer signatures of different surface types in deserts," *J. Geophys. Res.*, vol. 104, no. D10, pp. 12 147–12 158, 1999.

[16] G. Macelloni, S. Paloscia, P. Pampaloni, and E. Santi, "Global scale monitoring of soil and vegetation using SSM/I and ERS wind scatterometer," *Int. J. Remote Sens.*, vol. 24, no. 12, pp. 2409–2425, 2003.

[17] D. G. Long and M. R. Drinkwater, "Azimuth variation in microwave scatterometer and radiometer data over Antarctic," *IEEE Trans. Geosci. Remote Sens.*, vol. 38, no. 4, pp. 1857–1870, Jul. 2000.

[18] J. P. Hollinger, R. Lo, G. A. Poe, R. Savage, and J. L. Peirce, "Special Sensor Microwave/Imager user's guide," NASA Goddard Space Flight Center, Greenbelt, MD, 1987.

[19] J. P. Hollinger, J. L. Peirce, and G. A. Poe, "SSM/I instrument evaluation," *IEEE Trans. Geosci. Remote Sens.*, vol. 28, no. 5, pp. 781–790, Sep. 1990.

[20] C. Kummerow, W. Barnes, T. Kozu, J. Shiue, and J. Simpson, "The Tropical Rainfall Measuring Mission (TRMM) sensor package," *J. Atmos. Ocean Technol.*, vol. 15, pp. 808–816, Jun. 1998.

[21] E. D. McKee, *A Study of Global Sand Seas: Geological Survey Professional Paper 1052*. Washington, DC: U.S. Gov. Printing Office, 1979.

[22] F. Ulaby, R. Moore, and A. Fung, *Microwave Remote Sensing: Active and Passive*. Norwood, MA: Artech House, 1982, vol. 2.

[23] L. Tsang, J. A. Kong, and K.-H. Ding, *Scattering of Electromagnetic Waves: Theories and Applications*. New York: Wiley, 2000.

[24] C. A. Balanis, *Advanced Engineering Electromagnetics*. New York: Wiley, 1938.

Haroon Stephen (S'97) received the M.S. degree in remote sensing and geographic information systems from the Asian Institute of Technology (AIT), Bangkok, Thailand, in 1997. He is currently pursuing the Ph.D. degree in electrical engineering at Brigham Young University (BYU), Provo, UT.

From 1997 to 1998, he was with the European Space Agency office at AIT, where he investigated scatterometer applications for land surfaces. During this time he also taught short courses in remote sensing. He joined the Microwave Earth Remote Sensing Research Group at BYU in 1999. His current research interests are remote sensing of sand surfaces and tropical vegetation using spaceborne scatterometers and radiometers.

David G. Long (S'80–SM'98) received the Ph.D. degree in electrical engineering from the University of Southern California, Los Angeles, in 1989.

From 1983 to 1990, he was with the National Aeronautics and Space Administration (NASA) Jet Propulsion Laboratory (JPL), Pasadena, CA, where he developed advanced radar remote sensing systems. While at JPL, he was the Senior Project Engineer on the NASA Scatterometer (NSCAT) project, which was flown aboard the Japanese Advanced Earth Observing System (ADEOS) from 1996 to 1997. He was also the Experiment Manager and Project Engineer for the SCANSCAT scatterometer (now known as SeaWinds). In 1990, he joined the Department of Electrical and Computer Engineering, Brigham Young University (BYU), Provo, UT, where he currently teaches upper division and graduate courses in communications, microwave remote sensing, radar, and signal processing, is the Director of BYU's Center for Remote Sensing, and is the Head of the Microwave Earth Remote Sensing Laboratory. He is the Principal Investigator on several NASA-sponsored interdisciplinary research projects in microwave remote sensing and innovative radar systems. He has numerous publications in signal processing and radar scatterometry. His research interests include microwave remote sensing, radar, polar ice, signal processing, estimation theory, and mesoscale atmospheric dynamics. He has over 250 publications in the open literature.

Dr. Long has received the NASA Certificate of Recognition several times. He is an Associate Editor for the IEEE GEOSCIENCE AND REMOTE SENSING LETTERS.